Ultramicroscopy 227 (2021) 113298

Contents lists available at ScienceDirect

Ultramicroscopy

journal homepage: www.elsevier.com/locate/ultramic

Quantifying the performance of a hybrid pixel detector with GaAs:Cr sensor for transmission electron microscopy

Kirsty A. Paton [a,*], Matthew C. Veale [b], Xiaoke Mu [c], Christopher S. Allen [d,e], Dzmitry Maneuski [a], Christian Kübel [c,f], Val O'Shea [a], Angus I. Kirkland [d,e], Damien McGrouther [a]

[a] Scottish Universities Physics Alliance, School of Physics and Astronomy, University of Glasgow, G12 8QQ, UK
[b] UKRI Science & Technology Facilities Council, Rutherford Appleton Laboratory, Didcot, OX11 0QX, UK
[c] Karlsruhe Nano Micro Facility, Karlsruhe Institute of Technology, Hermann-von-Helmholtz-Platz 1, 76344, Eggenstein-Leopoldshafen, Germany
[d] Department of Materials, University of Oxford, Parks Road, Oxford, OX1 3PH, UK
[e] electron Physical Sciences Imaging Centre (ePSIC), Diamond Lightsource Ltd., Didcot, OX11 0DE, UK
[f] Department of Materials and Earth Science, Technische Universität Darmstadt and Karlsruhe Institute of Technology, Otto-Berndt-Str. 3, 64287 Darmstadt, Germany

ARTICLE INFO

Dataset link: http://dx.doi.org/10.5525/gla.researchdata.1145

Keywords:
Direct electron detector
DQE
MTF
Hybrid pixel detector
Transmission electron microscopy

ABSTRACT

Hybrid pixel detectors (HPDs) have been shown to be highly effective for diffraction-based and time-resolved studies in transmission electron microscopy, but their performance is limited by the fact that high-energy electrons scatter over long distances in their thick Si sensors. An advantage of HPDs compared to monolithic active pixel sensors is that their sensors do not need to be fabricated from Si. We have compared the performance of the Medipix3 HPD with a Si sensor and a GaAs:Cr sensor using primary electrons in the energy range of 60–300 keV. We describe the measurement and calculation of the detectors' modulation transfer function (MTF) and detective quantum efficiency (DQE), which show that the performance of the GaAs:Cr device is markedly superior to that of the Si device for high-energy electrons.

1. Introduction

The development of direct electron detectors (DEDs) over the past twenty years has opened up new experimental possibilities in electron microscopy, leading to significant advances in various fields [1,2]. Key to this success is increased sensitivity to incident electrons, which facilitates electron counting, compared to indirect scintillator-coupled detectors. This is invaluable when the total number of electrons to which the sample can be exposed is low (with the most demanding experiments requiring this be $\leq$ 10 $e^-/Å^2$) and also highly advantageous when performing quantitative analysis [3–5]. DEDs can be broadly divided into two categories: hybrid pixel detectors (HPDs) and monolithic active pixel sensors (MAPS). The latter have had great impact, substantially improving the resolution limit of cryogenic electron microscopy (cryoEM) at higher ($\geq$ 200 kV) accelerating voltages [6,7].

However, the former are more suitable for applications requiring electron counting with high frame-rates, a linear response to high electron flux and radiation hardness. HPDs consist of an application specific integrated circuit (ASIC), which contains the signal-processing and readout electronics, bump-bonded to a thick ($\geq$ 300 μm) sensor that protects the ASIC from the incident electrons, making them highly radiation resilient. On-pixel signal processing circuitry makes them capable of high (typically kHz) frame-rates and electron counting at MHz rates [8,9]. This makes them highly effective sensors for capturing fast (1 ms) dynamics in a conventional transmission electron microscope (TEM) [10], and they show the potential to record processes at timescales of $\leq$ 1 μs [11,12]. Their ability to maintain a linear response even when subjected to high ($\geq$ 1000 e^-/pixel/s) electron flux means they are suitable for use in a variety of diffraction-based experiments [9]. They have been successfully used for micro-electron diffraction (microED) in structural biology [13] and 4D scanning transmission electron microscopy (4D-STEM), in both convergent and nano beam electron diffraction modes [14–16] in materials science. Beyond this, they have facilitated the application of 4D-STEM to biological samples [17,18] and are promising for use in electron energy-loss spectroscopy [19].

Neither type of DED is capable of maximum performance across the full range of incident electron energies available on current generation TEM instruments (60–300 keV). MAPS devices consist of a thin Si sensor, $\leq$ 50 μm in thickness, and minimal on-pixel electronics, which means they have small, usually < 15 μm in pitch, pixels [20].

* Corresponding author.
E-mail address: kirsty.paton@glasgow.ac.uk (K.A. Paton).

https://doi.org/10.1016/j.ultramic.2021.113298
Received 29 September 2020; Received in revised form 1 February 2021; Accepted 24 April 2021
Available online 29 April 2021

High-energy (≥ 200 keV) electrons are transmitted through their thin sensors with minimal backscatter and there is little lateral spread in the signal produced by the small amount of energy that they deposit in the sensor [21–23]. These factors mean they offer excellent imaging performance for high-energy electrons, making them the detector of choice for high-energy cryoEM. At lower (≤120 keV) electron energies, their performance deteriorates due to increased lateral scatter in and backscatter from the sensor, making them less suitable for low-energy cryoEM [24,25] and studies of materials sensitive to sputtering damage [26,27]. MAPS detectors count electrons by identifying pixel clusters in sparsely populated frames, so that their count-rate is dependent on their frame-rate. A number of commercially available MAPS devices operate at kHz frame rates when binning frames or when reading out a reduced region of the sensor, though the recently developed 4D Camera can read out full frames at a rate of 87 kHz without binning [28]. This has the drawback of producing large volumes of empty data that are computationally expensive to manage and process. Newer HPDs are able to operate in a data-driven mode whereby only those pixels that record a hit are read out, reducing the size of the datasets that are produced [29]. The maximum electron fluence to which monolithic device can be exposed is also limited by the radiation hardness of their on-pixel electronics [3,30,31].

HPDs, such as Medipix3 [32], have been shown to match and even surpass the modulation transfer function (MTF) and detective quantum efficiency (DQE) of a conceptual square-pixel detector that counts all incident electrons only in the entry pixel, when used with low-energy electrons [33]. However, in sensors sufficiently thick to protect the ASIC, high-energy electrons travel long distances and are counted by multiple pixels, causing a degradation in performance [13,34]. The lateral scattering and penetration depth of an incident electron is inversely proportional to the average atomic number (Z) of the sensor. Unlike monolithic devices, HPDs can have sensors made of materials other than Si (Z = 14). HPDs with high-Z sensors should be capable of improved imaging performance for incident electrons across a wider range of energies, as the spatial distribution of the signal produced by high-energy electrons should be more localised [35]. This would increase the versatility of HPDs and, combined with their advantages relative to MAPS detectors, they would have the potential to be near "universal" detectors for transmission electron microscopy, suitable for almost all applications at all accelerating voltages.

Increasing the Z of the sensor may also have a negative impact on performance due to increased backscatter [36]. In this article, we investigate the extent to which the performance of HPDs can be improved by using a high-Z, specifically a GaAs:Cr (average Z = 32), sensor. We begin by describing in detail procedures suitable for performing measurements of the MTF and DQE of HPDs, for the purpose of characterising their imaging performance. We then compare the imaging performance of 500 μm thick GaAs:Cr and Si sensors bonded to Medipix3 ASICs for electrons at energies of 60–300 keV. Finally, we offer a comparison of their performance under uniform illumination and discuss some of the challenges associated with the use of high-Z sensors for imaging applications.

2. Detector structure

The Medipix3RX ASIC (henceforth referred to as Medipix3) consists of an array of 256 × 256 55 μm pitch pixels [32]. The signal-processing circuitry present on each pixel has an analogue front-end and a digital back-end. In the analogue section, the charge induced in a pixel due to an incident electron is amplified and converted into a shaped voltage pulse. When the detector is operating in single-pixel mode (SPM), this is registered as a hit if it surpasses a user set threshold, and one of the Linear Feedback Shift Registers in the digital back-end is incremented. During readout of a frame, the register acts as a shift register to readout the number of hits it has recorded during data acquisition. Used with the Merlin readout system [37], the detector is capable of frame rates greater than 1 kHz depending on counter bit-depth, with on-pixel count rates being determined by the ASIC settings [8]. The digital back-end contains two registers and up to two thresholds, TH0 and TH1 can be set. Alternatively, a single threshold can be used, with the two registers working in tandem such that while one is acting as a counter the other is operating as a shift register, permitting continuous acquisition of data with no gap time between frames.

The detector's other main mode of operation, is a charge summing mode (CSM), where neighbouring pixels pool their individual signal-processing circuitry and attempt to allocate incident electrons to a single pixel. Each pixel compares the voltage pulse produced in its analogue front end to TH0 but also sends copies of this pulse to summing nodes that are effectively located at its corners. At each node, the voltage pulses produced by the four pixels that share a corner are summed. If the summed voltage pulses surpass TH1, then the counter of the pixel identified has having the largest share of the deposited energy is incremented. The pixel which registers the most energy is identified as the pixel where the voltage pulse drops below TH0 last, as the time the voltage pulse is above TH0 is proportional to the energy deposited on the pixel.

The vast majority of room temperature semiconductor sensor materials are binary or ternary compounds, such as GaAs:Cr, CdTe and CdZnTe. The growth and fabrication of sensors from these materials is challenging and the presence of crystal defects and impurities can be common. These issues can lead to challenges such as incomplete charge collection, polarisation due to the build-up of trapped charge, high leakage currents, electric field instabilities and limitations in the sensor volumes that can be produced [38–40]. In recent years, however, technologies for manufacturing high-Z sensors that can operate at room temperature and for bonding these to ASICs have matured. The GaAs:Cr material that we have characterised represents a significant step forward compared to earlier forms of semi-insulating GaAs that have been investigated for use in imaging detectors [41,42]. It has been used with a variety of ASICs, including the Medipix3 ASIC, for X-ray imaging [43–45] and has been shown to be sufficiently robust for high-flux X-ray imaging [46].

In the case of the GaAs:Cr device that we have characterised, the sensor was bonded to the ASIC using a cold-weld indium bump-bonding process [47], and had a Ni front-side contact. Due to the electron mobility-lifetime product of GaAs:Cr being better than the hole mobility-lifetime product [44], the ASIC was set to collect electrons, and a negative bias of 300 V was sufficient to ensure complete collection of the electrons without any being lost due to trapping [43]. The Si detector consisted of high resistivity n-type Si with p+ on n implants that was bump-bonded using a standard solder bump-bonding process with an Al front-side contact. The Si sensor was operated with a positive bias of 110 V, with the ASIC set to collect holes. Both devices were cooled passively, and their typical operational temperatures were approximately 28 °C.

3. Characterisation of detector performance

The performance of an imaging detector can be characterised through the measurement of independent and dependent parameters. Independent, directly measurable quantities include the MTF, which quantifies the ability of a detector to transfer contrast in an image as a function of spatial frequency, ω. This is the Fourier space representation of a detector's point spread function (PSF), which describes the detector's average response to an idealised input signal with the form of a δ-function. The noise power spectrum (NPS) is another independent parameter that measures how a detector transfers the noise present in the image incident upon it. Dependent on both of these quantities, the detector's DQE describes the extent to which that detector reproduces the signal-to-noise ratio (SNR) of features in the images it records as a function of their spatial frequency.

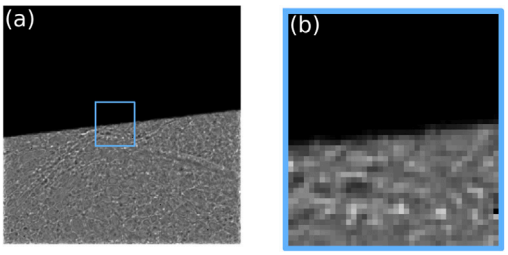

Fig. 1. (a) Mean image of the knife-edge recorded using a GaAs:Cr sensor operating in SPM with 300 keV electrons and (b) close-up of the region marked in (a) which was used to measure the ESF. No flat field correction has been applied to (a) or (b) so that the defects present in the region used to calculate the MTF can be clearly seen. The detector's counting threshold was set to 12.7 keV.

For pixelated, digital detectors, it is necessary to distinguish between the presampling and digital forms of these measures of detector performance. The presampling versions describe the detector's response without the effects of discrete sampling by pixels. In HPDs, they describe how noise and signal are affected by the interactions of the primary electron with the sensor due to the scatter of the primary electron itself, the production of any secondary X-rays or electrons, and by the lateral spread of signal-carriers produced by the primary electron and any secondary radiation as they travel to the pixel electrodes. The presampling forms also account for integration over the effective pixel area. For a detector that counts all incident electrons only in the entry pixel, the effective pixel area is equivalent to the physical pixel area. However, it can be smaller than the physical pixel if electrons are not counted when they enter the sensor in certain regions of a pixel (e.g. the corner or edge) or greater than the physical pixel if multiple pixels count an incident electron. The ratio of the effective pixel area to the physical pixel area is the detector's fill factor.

The digital MTF, NPS and DQE are their respective presampling form evaluated at the centre of each pixel [48]. The finite size of the pixels means that aliasing of the digital MTF and NPS is possible, due to undersampling, causing them to be overestimated at high ω [49]. Various approaches have been used to determine the MTF and DQE of imaging detectors for use in electron microscopy [34,36,50,51], in part because it is necessary to treat different types of pixelated detectors in different ways. In the interests of ensuring our results can be readily compared with those characterising other imaging detector types, and with a view to clarifying what constitutes best practice in performing these measurements for HPDs in electron microscopy, we outline our approach for calculating the MTF, NPS and DQE and the justifications for it.

The presampling MTF can be measured directly if the experimental method used oversamples the input signal that approximates a δ-function incident on the detector. We have used the well-established knife-edge method [50], informed by the approaches other authors have used when applying the technique to HPDs [13,34]. Fig. 1 shows an example knife-edge image recorded by a GaAs:Cr sensor. The knife-edge was set at an angle of 7° relative to the pixel rows such that the transition from the obscured portion of the pixel columns to the illuminated could be oversampled. A region of the knife-edge without defects 40 pixels wide was identified. For each column of pixels perpendicular to the edge in this region, the knife-edge location was identified with sub-pixel accuracy via interpolation as the position at which the intensity was equal to half the difference between the average intensity in the illuminated and covered regions of the sensor, as measured away from the location of the knife-edge. Pixel values were then rearranged in order of their distance from the position of the knife-edge to give a single, oversampled edge-spread function (ESF). The ESF can be differentiated directly to find the detector's line-spread function (LSF), which is equivalent to the PSF in one dimension, or it can be fitted with a function to minimise the effects of noise in the measurement. In many cases, though not all, the ESF can be fit with a function that consists of a sum of (complementary) error functions [52,53]. We have found that a single error function, as defined in Eq. (1), provided a good fit to the ESF, which is in agreement with the methods used by other authors for characterising HPDs [13,34] The MTF was then calculated as the modulus of the Fourier transform of the LSF that is calculated from differentiating ESF_{fit}.

$$\mathrm{ESF}_{fit}(x) = \frac{\mathrm{A}}{2}\left(1 + \mathrm{erf}\left(\frac{\mu - x}{\sigma}\right)\right) \tag{1}$$

In Eq. (1), μ is the mean position of the function, which is set to 0, σ is the width of the error function and A is a normalisation factor. Some studies include a term to correct for the effects of integrating over the physical pixel area or apply a correction directly to the MTF [50], but this has been shown to have a minimal effect on the final MTF [36] and was found to yield no significant improvement in the fit of our ESF.

It is not possible to oversample the noise profile of the detector and identify the aliased contributions from above the detector's Nyquist frequency (ω_N), which is its maximum sampling frequency and equal to 1/(2×pixel pitch). Consequently, the presampling NPS cannot be recovered. A correction for aliasing has been proposed for CCD cameras [50]. Undersampling and aliasing are inevitable for scintillator-coupled CCD cameras as electrons can be registered by multiple pixels in spite of the CCD pixel fill factor being < 1 [54], but this is not true for all pixelated detectors. The effective pixel area of HPDs can be larger than the physical pixel as incident electrons can be counted by multiple pixels, and they can therefore have an effective fill factor > 1. This has the effect of an anti-aliasing filter [36]. When using a high threshold, such that each incident electron is counted by at most one pixel, the NPS should be independent of spatial frequency and it is not necessary to account for aliasing. We have therefore not attempted to apply any correction for aliasing when calculating the NPS.

$$\mathrm{NPS}_{dig}(\omega_x, \omega_y) = \frac{x_0 y_0}{\mathrm{N}_x \mathrm{N}_y} E\left\{\left|\mathrm{FT}(\Delta d_{n_x,n_y})\right|^2\right\} \tag{2}$$

Eq. (2) provides a practical definition of the digital NPS of an imaging detector used in our calculations [48]. N_x N_y are the number of pixels in the detector's x and y-axis, while x_0 and y_0 are the pixel pitch in x and y. The value represented by $\Delta d_{n_x,n_y}$ is the difference between the number of counts registered by a pixel with coordinates (x, y) given a mean number of incident electrons per pixel n and the expectation value of the number of counts recorded by the pixel. This was measured by recording a series of flat field exposures, calculating their mean image and subtracting this from each frame in the series. The Fourier transform of each image was then calculated, and the square modulus of these were averaged to find the 2D NPS. The 1D digital NPS was then found by taking the radial average.

$$\mathrm{DQE}_{dig}(\omega) = \frac{d_n^2 \mathrm{MTF}_{pre}^2(\omega)}{n\ \mathrm{NPS}_{dig}(\omega)} \tag{3}$$

The digital DQE is defined by Eq. (3), where d_n is the mean number of counts recorded per pixel and n is the mean number of electrons per pixel in the flat field images used to calculate the NPS. To find n, the beam current I is measured and a series of images with a frame time t are recorded, with the entirety of the beam incident on the detector. The detector gain factor, g, is calculated using Eq. (4), where d_{n_m} is the mean number of counts recorded by the mth pixel and N the total number of pixels. The value of n for the flat field exposures used to determine the NPS was then found by calculating d_n for these images using the fact that $n = d_n/g$.

$$g = \frac{\sum_{m=0}^{m=N-1} d_{n_m}\ e}{I\ t} \tag{4}$$

A difficulty encountered in calculating the NPS in the way outlined above is that the low-frequency NPS tends to be noisier as there are fewer pixels over which to average, with this tending to an extreme for

NPS(0). The standard solution to this is calculate NPS(0) separately. At first glance, it would seem that NPS(0) should be the variance, $\sigma^2_{d_n}$, of $\Delta d_{n_x,n_y}$. However, as electrons scatter over multiple pixels, there are correlations in the number of counts recorded by each pixel and the variance is not an accurate measurement of NPS(0). To find NPS(0), the images of $\Delta d_{n_x,n_y}$ were binned by progressively larger factors, b and the variance of the images, normalised by the square of the binning factor was evaluated. As b increases, $\sigma^2_{d_n}/b^2$ reaches a plateau as the correlations between neighbouring pixels are discounted, which is taken to be NPS(0) [36]. DQE(0) is then calculated using Eq. (5), which is then used in the calculation of DQE(ω) as per Eq. (6), where NNPS(ω) is NPS(ω) normalised to the independently calculated value of NPS(0).

$$\mathrm{DQE}_{dig}(0) = \frac{d_n^2}{n\ \mathrm{NPS}_{Dig}(0)} \tag{5}$$

$$\mathrm{DQE}_{dig}(\omega) = \mathrm{DQE}_{dig}(0)\frac{\mathrm{MTF}^2_{pre}(\omega)}{\mathrm{NNPS}_{dig}(\omega)} \tag{6}$$

Measurements using electrons with energies in the range of 60–200 keV for both Si and GaAs:Cr detectors were performed by mounting the detectors on an FEI Tecnai T-20 TEM using the 35 mm port above the viewing screen. The beam current for these measurements was recorded using a Faraday cup mounted at the end of the chassis containing the detector, which was connected to a Keithly 485 Picoammeter. To acquire 300 keV electron data, the GaAs:Cr detector was mounted on the Gatan camera block on a FEI Titan 80–300 (S)TEM. For this set of measurements, the beam current was calculated using the number of counts registered by a Gatan Ultrascan located in the same plane as the Medipix3 device and the manufacturer-provided conversion factor.

The detector thresholds, TH0 and TH1 when operating in SPM and CSM respectively, were calibrated using fluorescence X-rays from a series of targets. This provides an absolute energy calibration, as low-energy photons typically deposit their energy in a single interaction, rather than scattering over multiple pixels as is the case for high-energy electrons. Consequently, the disparity between the maximum amount of energy deposited in a pixel by incident electrons and the initial energy of incident electrons is apparent. As the energy of the incident electrons increases, the maximum amount of energy deposited on a single pixel as a fraction of the primary electron energy decreases, due to increased scatter. This effect is more pronounced when in SPM, as in CSM the energy deposited over 2 × 2 pixel blocks by incident electrons is summed. A result of this is that the maximum threshold at which it was possible to fit the knife-edge data with Eq. (1) is lower than the counting threshold that corresponds to the primary electron energy, substantially so for electrons with energies ≥ 120 keV. For example, for the 300 keV electron data acquired with a GaAs:Cr device, the maximum amount of energy deposited on a single pixel when the detector was working in SPM was 160 keV, and the highest threshold at which it was possible to fit Eq. (1) was lower than this (131.3 keV), due to insufficient counts being recorded at thresholds close to 160 keV.

4. MTF and DQE measurements

Figs. 2 and 3 show MTFs and DQEs obtained using the lowest threshold above both detectors' noise levels; a threshold equal to half the primary electron energy and the highest threshold common to both devices at which the knife-edge data could be fit with Eq. (1) for 60 keV and 80 keV electrons respectively. The MTFs of the Si device in Fig. 2(a) are slightly lower than those of the GaAs:Cr device in 2(c) for a given threshold. However, in Fig. 2(b), the Si DQEs are significantly higher than their GaAs:Cr counterparts in 2(d). Comparing the MTFs of the Si detector for 80 keV electrons in Fig. 3(a) with those of the GaAs:Cr detector in 3(c), the performance of the latter is marginally better. As was the case at 60 keV, the DQEs of the Si detector seen in Fig. 3(b) are again significantly higher than those of the GaAs:Cr detector in 3(d).

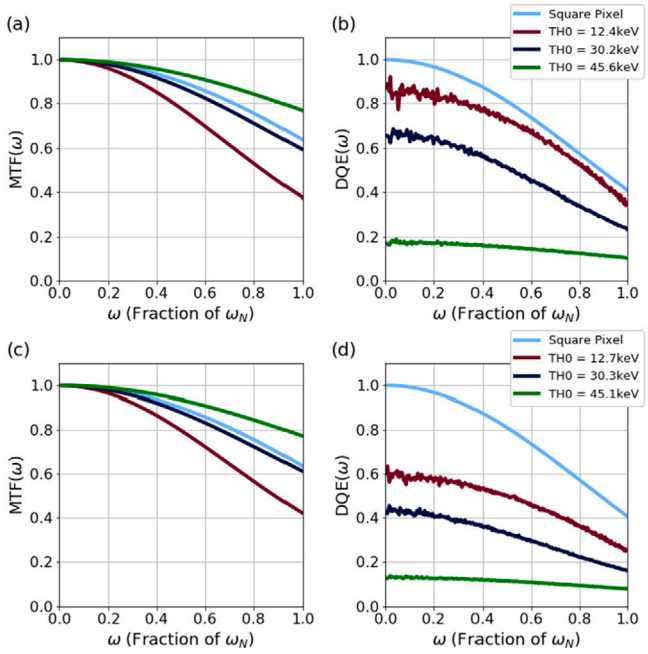

Fig. 2. (a) MTF and (b) DQE measurements using selected thresholds for a Si device operating in SPM for 60 keV electrons; (c) MTF and (d) DQE measurements for a GaAs:Cr detector under the same conditions.

In the case of the MTF measurements in Figs. 2 and 3 the difference between the two sensors decreases with increasing threshold and tends to increase with increasing ω. The greatest difference in MTF for both the 60 keV and 80 keV electrons occurs when a low threshold is used at high values of ω. Table 1 summarises the key values and differences between the low threshold MTF and DQE measurements presented in Figs. 2 and 3, including the low threshold values of MTF(ω_N). While the difference in DQE between the two sensors also decreases with threshold, the difference also tends to decrease, rather than increase, with increasing ω. This is made apparent by considering the low threshold values of DQE(0), DQE($0.5\omega_N$) and DQE(ω_N) in Table 1 for 60 keV and 80 keV electrons, as well as the values of ω at which the maximum and minimum differences in DQE occur.

A common benchmark for imaging detector performance is the MTF and DQE of a detector with square pixels that counts all incident electrons in the entry pixel only. Such a detector has a PSF with the form of a top-hat function, unitary gain and a constant NPS. These factors give rise to a MTF that is a sinc function equal to 0.64 at ω_N and, per Eq. (3), a DQE that is the square of the MTF, with a value of 0.41 at ω_N [51]. These are plotted in Figs. 2 and 3 for comparison with the experimental results. However, counting the primary electron in multiple pixels is a deterministic blurring process by which both the MTF and NPS are suppressed. In cases where the NPS is aliased, the NPS can be suppressed to a greater extent than the MTF is, as the aliased terms are preferentially suppressed [36]. This causes an increase in the DQE, particularly at high spatial frequencies, an effect which is illustrated in Fig. 3(b) for the low-threshold DQE of the Si sensor.

In Fig. 4 MTF(ω_N) as a function of threshold for both detectors when operating in SPM and CSM for 60 keV and 80 keV electrons is plotted. For both detectors in SPM, the value of MTF(ω_N) increases with the counting threshold. This is consistent with the expectation that the effective pixel area decreases with increasing counting threshold [33,34]. At low thresholds, the effective pixel size is larger than the physical pixel pitch and a pixel can count an incident electron even if the electron is not incident on that pixel, causing a reduction in the MTF. The higher the counting threshold, the more energy an electron must deposit in a pixel to be counted by that pixel, decreasing the effective

Table 1
Comparison of key values summarising the low threshold MTF and DQE measurements presented in Figs. 2, 3, 7, 8 and 9. The maximum and minimum differences in DQE ('Max. Diff. DQE' and 'Min. Diff. DQE' respectively) are calculated by subtracting the GaAs:Cr DQE from the Si DQE data so that a negative value indicates that the GaAs:Cr DQE is greater than the Si DQE.

Energy (keV)	Sensor	MTF(ω_N)	DQE(0)	DQE(0.5ω_N)	DQE(ω_N)	Max. Diff. DQE	Min. Diff. DQE
60	Si	0.38	0.87	0.73	0.35	0.33 (0.02ω_N)	0.09 (.99ω_N)
	GaAs:Cr	0.42	0.60	0.50	0.25		
80	Si	0.31	0.96	0.81	0.37	0.32 (0.05ω_N)	0.06 (ω_N)
	GaAs:Cr	0.38	0.74	0.63	0.31		
120	Si	0.14	0.85	0.55	0.11	−0.42 (0.87ω_N)	0.00 (0.16ω_N)
	GaAs:Cr	0.38	0.80	0.73	0.50		
200	Si	0.01	0.80	0.17	0.00	−0.74 (0.71ω_N)	−0.07 (0.02ω_N)
	GaAs:Cr	0.26	0.91	0.79	0.51		
300	GaAs:Cr	0.04	0.80	0.34	0.02	–	–

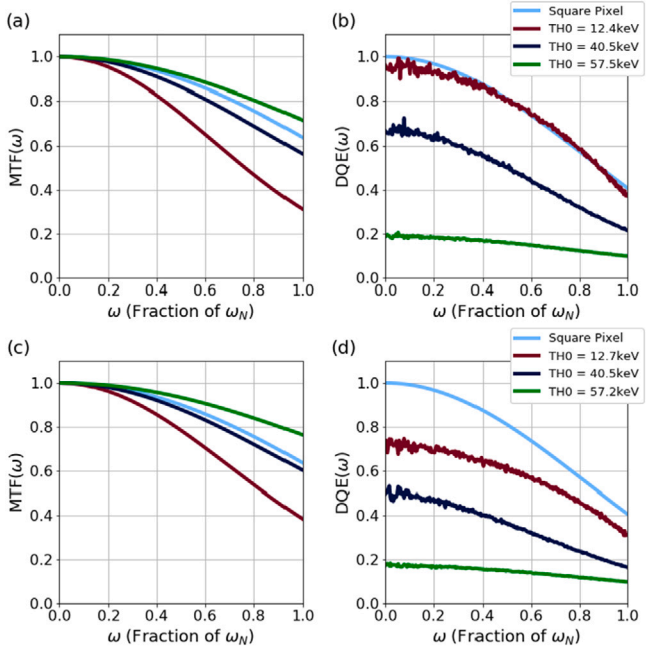

Fig. 3. MTF for (a) Si and (c) GaAs:Cr detectors operating in SPM with selected counting thresholds for 80 keV electrons; the corresponding DQE results for (b) the Si device and (d) the GaAs:Cr device.

pixel size. Consequently, the value of MTF(ω_N) can exceed 0.64 at high thresholds, as the effective pixel is smaller than the physical pixel pitch of the detector, though ω_N remains fixed by the physical pixel pitch.

The 60 keV results for the two devices operating in SPM in Fig. 4(a) highlight that the GaAs:Cr device outperforms the Si detector at low counting thresholds, with the MTF of the two devices converging at high thresholds. The difference at low counting thresholds is small, with a maximum value of 0.06 when the GaAs:Cr detector has a threshold of 14.6 keV. At 80 keV, the GaAs:Cr consistently outperforms the Si detector across all counting thresholds. The difference in MTF(ω_N) between the two devices decreases with increasing threshold, with a maximum difference of 0.1 and a minimum difference of 0.07.

When operating in CSM, the performance of the two devices is very different, with MTF(ω_N) being independent of counting threshold in Fig. 4(b). This follows from the fact that whether or not an electron is counted depends on the sum of the charge induced in neighbouring pixels. For low-energy electrons, which typically deposit all their energy across one of the 2 × 2 pixel blocks that the CSM algorithm operates across, this will be consistently above threshold until the threshold is equal to the energy of the incident electron. The extent to which MTF(ω_N) deviates from the ideal value of 0.64 is indicative of how successful the CSM algorithm is at identifying the entry pixel. There is minimal difference between the Si and GaAs:Cr detectors in CSM for 60 keV electrons, with MTF(ω_N) fluctuating around 0.53 for both devices. For 80 keV electrons, the GaAs:Cr detector marginally outperforms the Si detector, with MTF(ω_N) varying between 0.53 and 0.54 for the former and fluctuating around 0.5 for the latter.

The dependence of DQE(0) and DQE(ω_N) on threshold for the two detectors in both modes of operation for 60 keV and 80 keV electrons is shown in Figs. 5 and 6. These results make apparent the difference in performance between the two detectors when using electrons at these energies. When the detectors operate in SPM, DQE(0) decreases gradually with increasing threshold up to approximately half the primary electron energy, but at thresholds above this, DQE(0) decreases rapidly as the counting threshold is increased. The CSM DQE(0) in Fig. 5(b) exhibits a reduced negative dependence on threshold compared to the SPM DQE(0) results. DQE(ω_N) tracks the dependence of DQE(0) on threshold, although in the SPM results in Fig. 4(a) there is not an obvious change in dependence at half the primary electron energy. In CSM, DQE(ω_N) is approximately constant for both 60 keV and 80 keV electrons, with only minimal negative dependence on threshold seen in Fig. 6(b).

The negative dependence of the DQE on counting threshold seen in the SPM results arises from a similar reason as the positive dependence of MTF(ω_N) on counting threshold. As the effective pixel size decreases with increasing threshold, the likelihood of electrons not being registered by the detector increases, reducing the efficiency of the detector. It may seem as though the value of DQE(0) should be constant for all counting thresholds up to half the primary electron energy, as it is only when the threshold is equal to half the primary electron energy that the effective pixel size should be less than the physical pixel size, leading to electrons not being counted. In practice, as the electrons scatter through the sensor depositing their energy in multiple pixels, some electrons will not be registered at lower thresholds as they fail to deposit enough energy in any single pixel to be counted.

The relative constancy of DQE(0) and DQE(ω_N) as a function of threshold for the CSM results can be attributed to the same factors as the constancy of MTF(ω_N), namely that the signal recorded by neighbouring pixels is summed together. Nevertheless, there is still a gradual decrease in the value of DQE(0) and DQE(ω_N) with increasing counting threshold. This is most probably due to a small percentage of electrons that deposit their energy over an extended number of pixels greater than the 2 × 2 blocks of pixels that the CSM algorithm works across being discounted, as no single block of pixels has the full energy of the electron deposited in it. Another process that likely contributes to this dependence on threshold is the backscatter of some incident electrons, which do not deposit the entirety of their energy in the sensor.

At increasing electron energy, the benefits of the GaAs:Cr sensor become apparent. Fig. 7 shows the MTF and DQE for the Si and GaAs:Cr devices in SPM at 120 keV using the lowest and highest thresholds common to both detectors for which the knife-edge could be fit and the threshold closest to half the primary electron energy. Both the MTFs

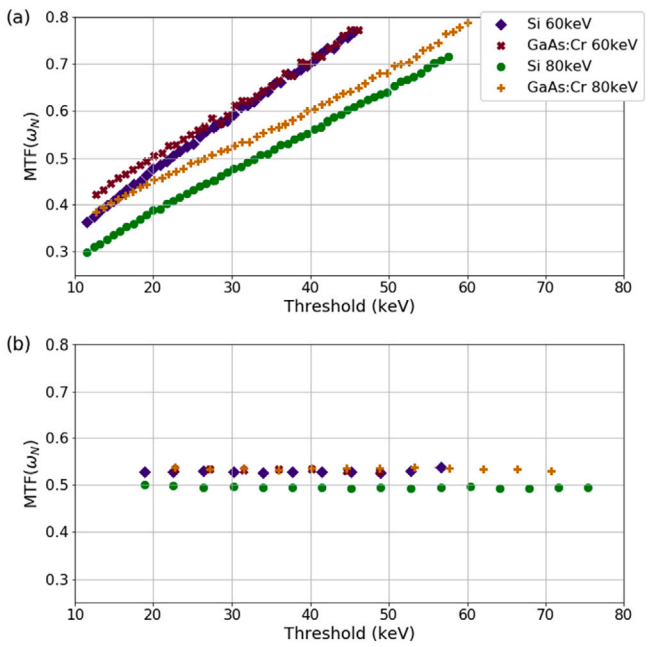

Fig. 4. MTF(ω_N) for Si and GaAs:Cr devices as a function of threshold for 60 keV and 80 keV electrons a when operating in (a) SPM and (b) CSM.

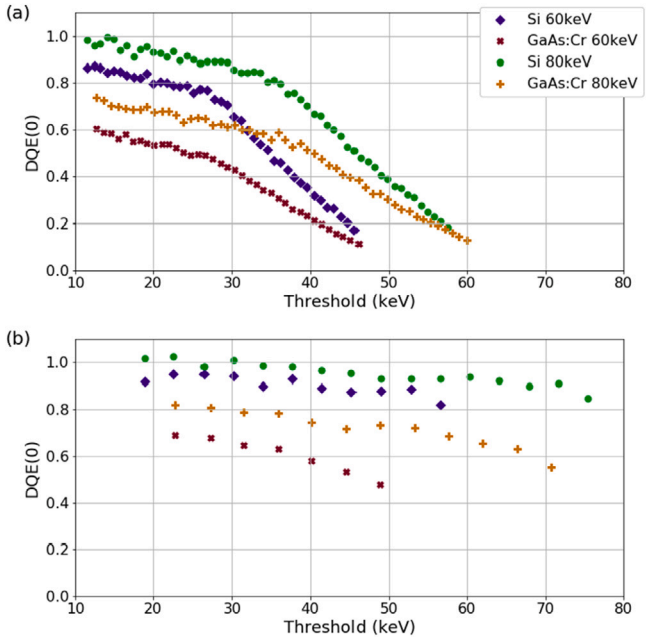

Fig. 5. DQE(0) as a function of threshold for Si and GaAs:Cr detectors for 60 keV and 80 keV electrons in (a) SPM, (b) CSM.

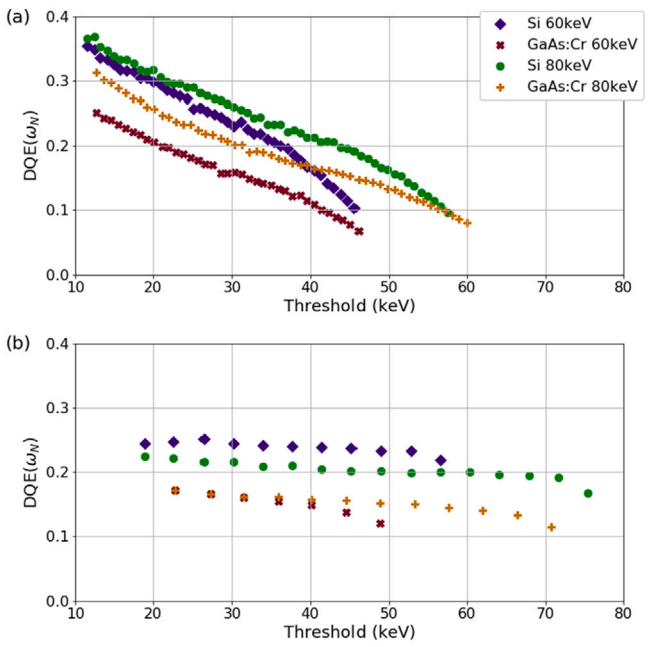

Fig. 6. Dependence of DQE(ω_N) on counting threshold for GaAs:Cr and Si devices operating in (a) SPM and (b) CSM, for electrons with energies of 60 keV and 80 keV.

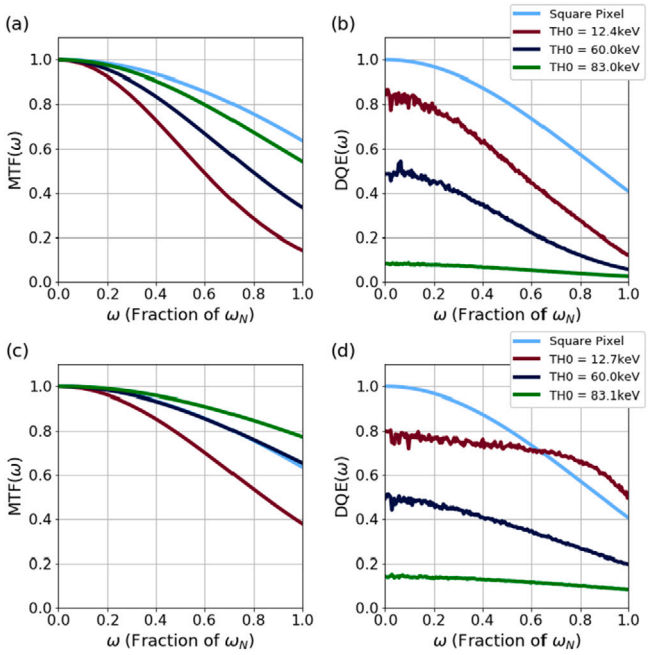

Fig. 7. (a) MTF and (b) DQE at selected thresholds for a Si device operating in SPM for 120 keV electrons; (c) MTF and (d) DQE for a GaAs:Cr detector in SPM for 120 keV electrons at selected thresholds.

and the DQEs of the GaAs:Cr device are superior to those of the Si detector. At each threshold shown in Figs. 7(a) and (c) the MTF of the GaAs:Cr device is at least 0.20 higher than the MTF of the Si device at ω_N. The greatest difference is 0.32 for the intermediate threshold MTF at ω_N, whereas the greatest difference in DQE occurs for the low threshold measurement, the key values of which are summarised in Table 1.

For 200 keV electrons the GaAs:Cr device clearly outperforms the Si detector in terms of both MTF and DQE. Fig. 8 shows the MTFs and DQEs of the two detectors operating in SPM for 200 keV electrons using the lowest threshold above the noise level of both detectors; the highest threshold common to both devices at which the knife-edge data could be fit and the threshold equal to half the highest threshold used for both devices. The different choice in thresholds shown in Fig. 8 compared to Figs. 2, 3 and 7 is due to the increased disparity between the maximum amount of energy deposited on a pixel and the primary electron energy when using higher-energy electrons discussed in Section 3. The greatest difference between the measurements in Figs. 8(a) and (c) occurs when using an intermediate threshold, at which the GaAs:Cr MTF is 0.54 greater than its Si counterpart at $0.64\omega_N$. In Figs. 8(b) and (d) the greatest difference in DQE is again when using a low threshold, with

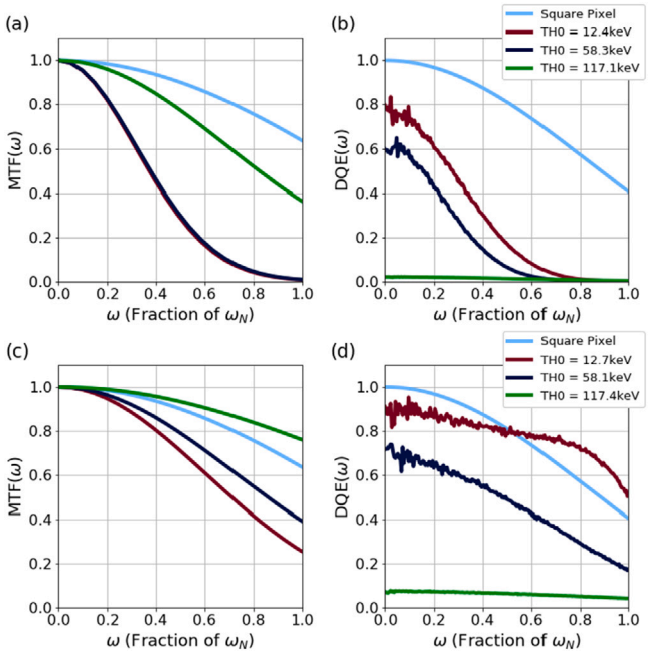

Fig. 8. 200 keV SPM (a) MTF and (b) DQE for a Si detector at selected thresholds and (c) MTF and (d) DQE measurements for a GaAs:Cr device at the similiar thresholds.

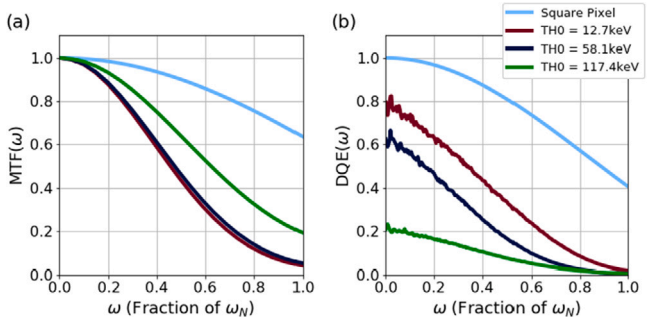

Fig. 9. (a) MTF and (b) DQE at selected thresholds for a GaAs:Cr Medipix3 device operating in SPM for 300 keV electrons.

values summarising the difference in performance noted in Table 1. However, unlike at lower electron energies, the difference in DQE continues to be significant at higher thresholds. For instance, the maximum difference between the intermediate threshold DQEs is 0.42 at $0.5\omega_N$, which is comparable with the maximum difference for the low threshold 120 keV DQE measurement in Table 1. Overall, the difference in performance between the GaAs:Cr and Si detectors is greater at 200 keV than it is at lower electron energies for which the performance of the Si detector is comparable to or greater than that of the GaAs:Cr detector.

In Figs. 7(d) and 8(d), the low threshold DQE of the GaAs:Cr detector for 120 keV and 200 keV electrons benefits from the anti-aliasing effect of the electron being counted by multiple pixels as was the case for the Si detector's low threshold DQE for 80 keV electrons in Fig. 3(b). Accounting for this effect, the maximum value of DQE(ω_N) that is possible is 0.5 [36]. The GaAs:Cr low threshold DQE(ω_N) in Figs. 7(d) and 8(d) is 0.50 and 0.51, which is in good agreement with this prediction. The greatest extent by which the low threshold DQE of the GaAs:Cr detector exceeds the expected DQE of a square pixel detector in the absence of anti-aliasing blur is by 0.12 at a spatial frequency of $0.9\omega_N$ for 120 keV electrons and by 0.17 at $0.86\omega_N$ for 200 keV electrons.

However, the performance of the GaAs:Cr detector deteriorates for 300 keV electrons. The MTFs and DQEs of the GaAs:Cr device for 300 keV electrons using the same thresholds used in Fig. 8 are shown Fig. 9. These make apparent the degradation in performance of the GaAs:Cr device, being comparable to the MTFs and DQEs of the Si device at 200 keV in Figs. 8(a) and (b). Consideration of the values summarising the low threshold MTF and DQE measurements for the Si detector for 200 keV electrons and the GaAs:Cr detector for 300 keV electrons in Table 1 indicates that the GaAs:Cr detector offers (in some respects) better performance at an accelerating voltage of 300 kV than the Si device offers at 200 kV.

Examination of the MTF(ω_N) as a function of threshold for 200 keV and 300 keV electrons in Fig. 10 confirms the similarity in performance between the Si detector for 200 keV electrons and the GaAs:Cr detector for 300 keV electrons. It also confirms the superiority of the GaAs:Cr detector MTF compared with the Si detector for 200 keV electrons for both modes of operation. In SPM, MTF(ω_N) for the GaAs:Cr detector for 200 keV and 300 keV electrons increases with threshold. For the Si detector MTF(ω_N) for 200 keV electrons initially decreases with threshold before increasing and surpassing the GaAs:Cr detector's response to 300 keV electrons in Fig. 10(a). In Fig. 10(b), the GaAs:Cr MTF(ω_N) for 200 keV electrons decreases with increasing threshold, whereas for 300 keV electrons it initially decreases before increasing and then decreasing again. For 200 keV electrons with the Si detector operating in CSM, MTF(ω_N) decreases to a minimum of 0.00 at a threshold of 109.3 kV before increasing at thresholds above 130 keV.

The various different trends in MTF(ω_N) as a function of threshold for the two devices for 200 keV and 300 keV electrons in Fig. 10 can all be attributed to the same principles that describe the low-energy electron MTF(ω_N), DQE(0) and DQE(ω_N) results in Figs. 4–6. The range of 200 keV electrons is sufficiently reduced in the GaAs:Cr detector such that the SPM MTF(ω_N) increases with increasing threshold, for the same factors that explain the low-energy SPM MTF(ω_N) dependence on threshold in Fig. 4(a). The dependence of MTF(ω_N) on threshold for 200 keV electrons and 300 keV electrons for the Si and GaAs:Cr devices operating in SPM can be explained by a combination of the increased ranges of 200 keV and 300 keV electrons in Si and GaAs:Cr respectively and the tendency of electrons to deposit more energy towards the end of their trajectory in the sensor rather than at the beginning [55,56]. Increasing the counting threshold does not initially improve the MTF (which is also apparent in Figs. 8(a) and 9(a)), as using a high threshold is more likely to count the electron in a pixel at the end of the electron's trajectory rather than the entry pixel. However, at very high thresholds, work with the Eiger detector [13] suggests that the only electrons counted are the small fraction of electrons that deposit most of their energy close to their entry point, causing an improvement in MTF.

Although 200 keV electrons have a sufficiently reduced range in GaAs:Cr such that in SPM using a high threshold successfully identifies the entry pixel of those electrons that are counted, they are still able to deposit their energy over multiple 2 × 2 pixel blocks. Consequently, when the GaAs:Cr sensor operates in CSM, multiple pixels register 200 keV electrons when using a low threshold. As the counting threshold increases, hits associated with the pixel block that has the most energy deposited on it continue to be counted, but this block does not necessarily contain the entry pixel. Increasing the counting threshold therefore suppresses hits associated with the block containing the entry pixel, which causes the decrease in MTF(ω_N) with increasing threshold seen in Fig. 10. This also explains the initial decrease seen in the 300 keV GaAs:Cr CSM MTF(ω_N) and 200 keV Si CSM MTF(ω_N). The increase in MTF(ω_N) at high threshold for both 300 keV electrons and the GaAs:Cr detector and 200 keV electrons and the Si detector in CSM occurs for the same factors as the improvement in their SPM counterparts at high threshold.

In Fig. 11, the trends in DQE(0) as a function of threshold for both devices are consistent with the interpretation of the MTF(ω_N) data above. Operating in SPM, the 200 keV DQE(0) for the Si and GaAs:Cr

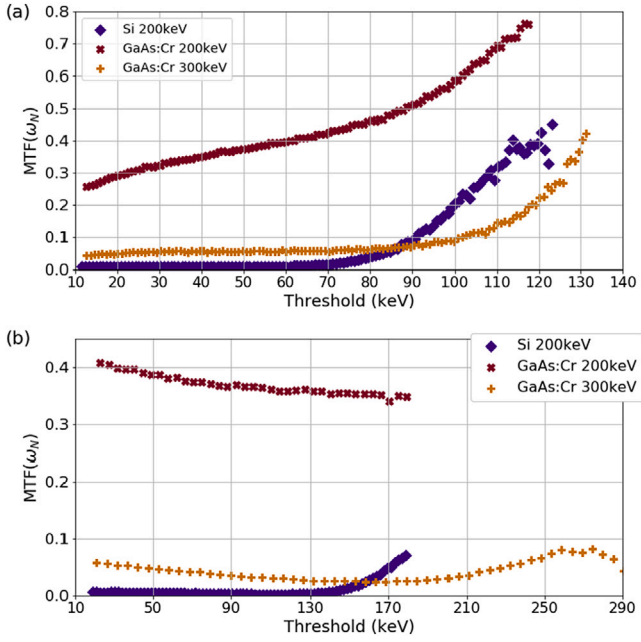

Fig. 10. Dependence of MTF(ω_N) on counting threshold for a Si detector for 200 keV electrons and a GaAs:Cr detector for 200 keV and 300 keV electrons in (a) SPM and (b) CSM.

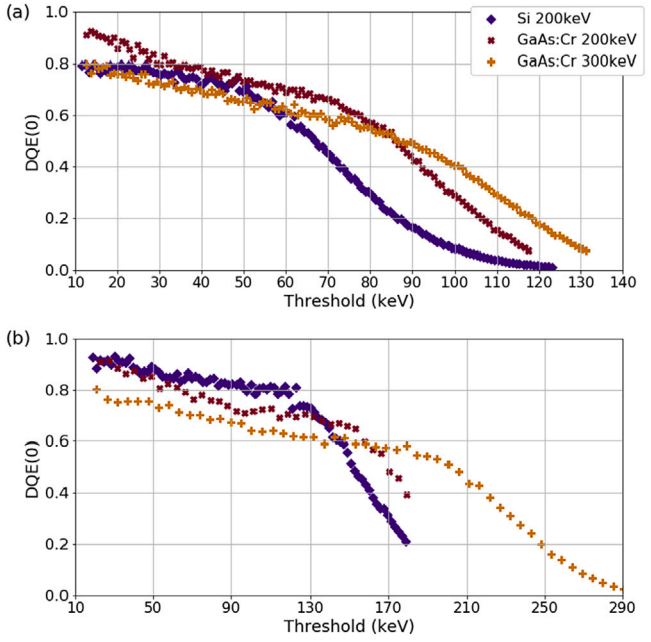

Fig. 11. DQE(0) as a function of counting threshold for a Si device with 200 keV electrons and a GaAs:Cr device for 200 keV and 300 keV electrons with the devices operating in (a) SPM (b) CSM.

detectors and the 300 keV DQE(0) for the GaAs:Cr detector in Fig. 11(a) exhibit a similar trend as to that seen for the low-energy SPM results in Fig. 5(a). The principle difference between the results in Figs. 5(a) and 11(a) is that in the latter the threshold at which there is a change in gradient in the dependence of DQE(0) on threshold is approximately half the maximum energy deposited by the primary electron on a single pixel, rather than approximately half the primary electron energy as in Fig. 5(a). The difference seen in the rate at which DQE(0) decreases with increasing threshold for the two detectors for 200 keV electrons can be attributed to the spread of the signal produced by 200 keV electrons being greater in the Si detector than it is in the GaAs:Cr detector. Consequently, more electrons deposit enough energy on a single pixel in the GaAs:Cr sensor to be counted for a given threshold than they do in the Si detector. That the high threshold value of DQE(0) for 300 keV electrons in the GaAs:Cr sensor is greater than the high threshold DQE(0) for 200 keV electrons in either device is due to both the reduced spread in signal in the GaAs:Cr sensor and the fact that the net energy that can be deposited by a 300 keV electron is greater than that deposited by a 200 keV electron.

When the detectors operate in CSM, there is a notable difference between the dependence of DQE(0) on threshold at high electron energies compared with at low electron energies. For the CSM DQE(0) in Fig. 11(b), there is a marked increase in the rate at which the value of DQE(0) decreases at high thresholds relative to the rate at which it decreases at low threshold. This is similar to the dependence of DQE(0) on threshold when the detectors operate in SPM, rather than the gradual decrease with increasing threshold seen at 60 and 80 keV (Fig. 5(b)), where any change in gradient is slight and difficult to discern. The difference between the low-energy and high-energy trends can be explained by the same factors that explain the dependence of MTF(ω_N) on threshold in Fig. 10(b). At low thresholds, the fraction of incident electrons that are counted decreases gradually with respect to threshold, as the incident electrons deposit their energy over multiple CSM pixel blocks and, in each block, the reconstructed charge needs to be above threshold for it to be counted. Above a certain counting threshold, electrons are only counted in a single pixel block and as the counting threshold increases the greater the energy deposited in

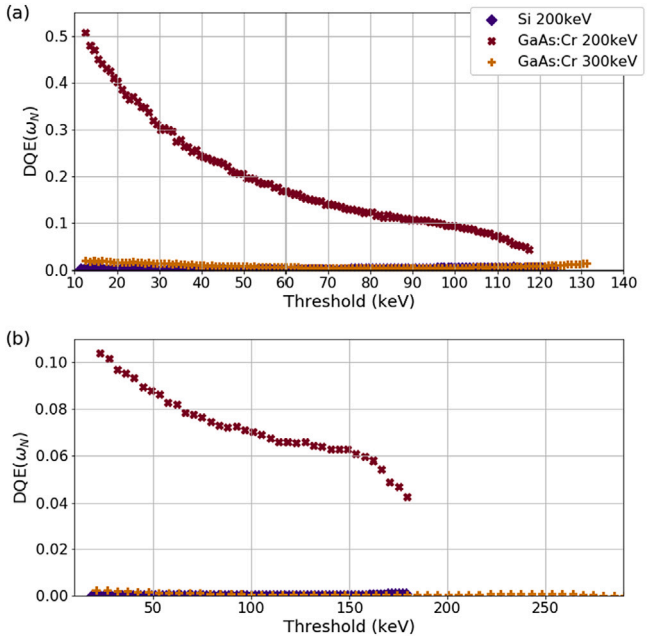

Fig. 12. DQE(ω_N) for a GaAs:Cr device for 200 keV and 300 keV electrons and a Si device for 200 keV electrons in (a) SPM and (b) CSM as a function of threshold.

that block must be for the electron to be counted. This is analogous to the detector behaviour in SPM, but with the added complication of how the electron energy is deposited over blocks of neighbouring pixels rather than in individual pixels. The thresholds at which the gradient of DQE(0) as a function of counting threshold changes for 200 keV electrons and the Si detector and 300 keV electrons and the GaAs:Cr detector are also the thresholds above which the corresponding MTF(ω_N) begin to rapidly increase with respect to threshold, corroborating the interpretation of the high threshold improvement in MTF in Fig. 10(b).

DQE(ω_N) as a function of counting threshold for the two detectors operating in SPM and CSM for high-energy electrons is shown in

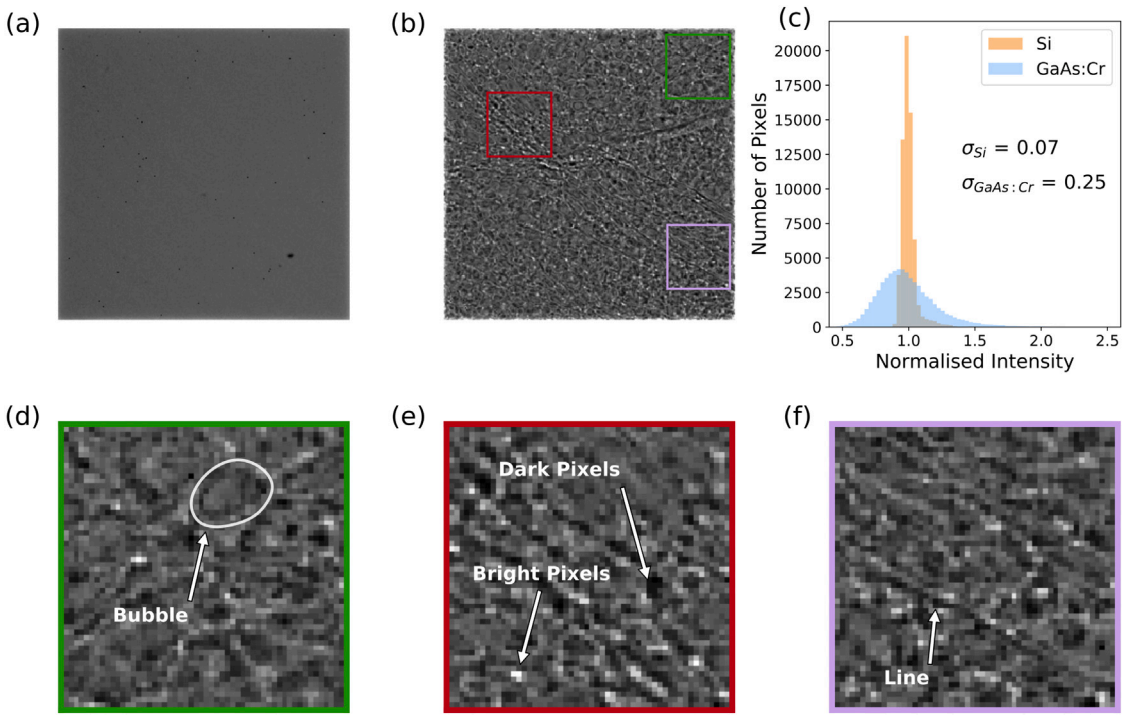

Fig. 13. Flat field images of (a) Si and (b) GaAs:Cr devices operating in SPM with 200 keV electrons normalised to their respective mean values; (c) histograms of the images in (a) and (b) with a note of the standard deviations of the intensity distributions; (d), (e) and (f) show close-ups of regions of the GaAs:Cr sensor indicated in (b), with various types of defects in the GaAs:Cr sensor highlighted. The contrast in all images has been adjusted such that the minimum and maximum intensities map to the limits of the normalised intensity plotted in (c).

Fig. 12. Consistent with the results in Figs. 10 and 11, the 200 keV DQE(ω_N) of the GaAs:Cr detector is significantly better than the 300 keV DQE(ω_N) of the GaAs:Cr detector and the Si detector 200 keV DQE(ω_N) in both modes of operation. In SPM, the GaAs:Cr DQE(ω_N) for 200 keV electrons decreases with threshold, tracking the dependence of DQE(0) on threshold. In contrast, the Si detector DQE(ω_N) for 200 keV electrons is 0.00 at low threshold, increasing to 0.01 at thresholds greater than 106.9 keV, while the GaAs:Cr detector DQE(ω_N) for 300 keV electrons initially decreases before increasing again. This behaviour reflects the fact that increasing the counting threshold initially does little to improve the MTF but does increase undercounting of incident electrons, while at very high thresholds the improvement in MTF at high ω outweighs the adverse impact of undercounting electrons on the DQE. The CSM DQE(ω_N) in Fig. 12(b) confirms the failure of the CSM algorithm to enhance detector performance for high-energy electrons in both sensors. At low thresholds, the CSM DQE(ω_N) of the GaAs:Cr detector is lower than the low threshold SPM DQE(ω_N). The Si detector CSM DQE(ω_N) for 200 keV electrons never exceeds 0.00 for all thresholds, and this is also true of DQE(ω_N) for the GaAs:Cr detector in CSM for 300 keV electrons.

5. The influence of defects on sensor performance

A difficulty in the fabrication of compound semiconductors are the defects that develop as part of the growth process [57,58]. Fig. 13 shows normalised flat field exposures of Si and GaAs:Cr devices. The Si sensor is homogeneous whereas the GaAs:Cr sensor displays a high number of features that range from small bubble-like structures to lines that extend across the full sensor. Examples of some of the structures that can be observed in the GaAs:Cr sensor are highlighted in Figs. 13(d) and (f). These features are indicative of defects in the sensor which result in non-uniformities in the electric field across the sensor and consequently the pixel matrix, causing distortions in both the shape and the size of the pixels. Areas of increased intensity indicate larger pixels, which count a disproportionate number of electrons while darker regions indicate pixels that are smaller and that have lost hits to neighbouring pixels. An example of a cluster of pixels that are larger than expected and therefore overcount is seen in Fig. 13(e). It should be noted that pixels that were identified as noisy due to damage, failure in the manufacture process etc. were masked prior to the image being acquired, so this is not the cause of the bright pixels such as those seen in Fig. 13(e). Histograms of the intensities in the normalised flat field images in Fig. 13(c) clearly show the broader range of intensities present in the GaAs:Cr flat field image compared with flat field image recorded by a Si device. The standard deviation of the range of intensities present in the GaAs:Cr flat field image is almost four times that of the flat field image recorded by the Si sensor in spite of the latter having a greater number of dead pixels. The variation in intensity in the Si flat field image is due to the slight dispersion of the threshold across the pixel matrix.

A standard procedure to correct for variation in intensity across a pixelated detector due to e.g. variation in the counting threshold across the pixel matrix is to apply a flat field, or gain, correction. In Figs. 14(a) and (b), images of a standard calibration sample recorded by a GaAs:Cr detector operating in SPM with and without a flat field correction are shown. The effect of applying a flat field correction can be seen from the line profiles taken across the normalised images with and without the correction in Fig. 14(d) as well as histograms of the images in Fig. 14(c). Comparing the line profiles extracted from the corrected and uncorrected images there is an improvement in the contrast present in the corrected image. In the case of the corrected image, the periodicity of the cross grating is apparent and can be readily measured as having a mean value of 43 pixels. This is not the case for the line profile extracted from the uncorrected image, where the additional variation in intensity makes the period of the cross grating difficult to discern. The mean value of both line profiles is 1.0, but while the standard deviation of the corrected image line profile is 0.09, that of the uncorrected image line profile is 0.14, an increase of more than 50%. This reflects the effectiveness in the flat field correction at reducing noise due to the sensor defects. Similarly, the range of intensities present in the

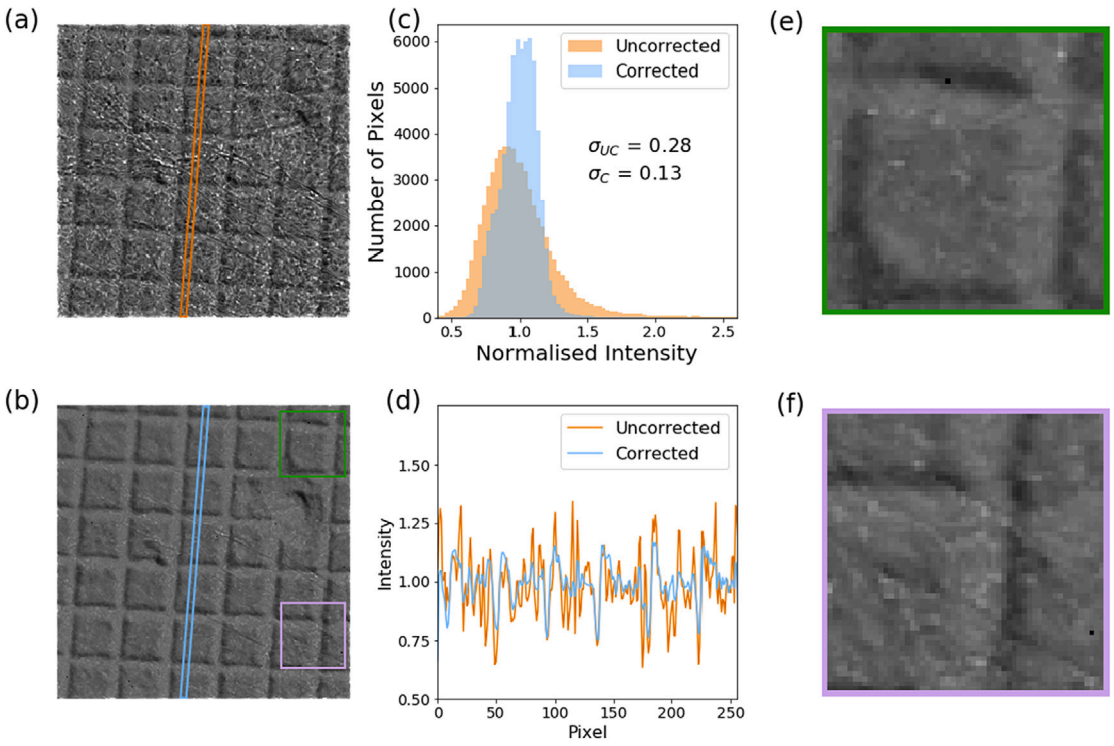

Fig. 14. Low-magnification images of a carbon cross grating with gold shadowing (Ted Pella) recorded with the GaAs:Cr sensor operating in SPM using 300 keV electrons (a) without a flat field correction applied and (b) with a correction applied, normalised by their respective mean value; (c) histograms of the images seen in (a) and (b), with the standard deviations of the normalised intensity distributions noted; (d) plots of the line profiles indicated by the region of interest marked in (a) and (b), the width of which is the integration width of the line profiles; (e) and (f) are close-ups of the regions of interest highlighted in (b). As in Fig. 13, the minimum and maximum intensities in the images are also the normalised intensity limits for the histograms seen in (c).

corrected image is reduced, with the standard deviation of the range of intensities in the corrected image being less than half that of the uncorrected image.

However, examination of the two regions of interest highlighted in Figs. 14(d) and (e), which correspond to the regions of the GaAs:Cr sensor seen in close-up in Figs. 13(d) and (f), show that the distortions present in the uncorrected images can still be seen in the corrected image. Increasing the counting threshold increased the visibility of the defects, which may be due to a reduction in blurring due to the improved detector PSF at higher counting thresholds. Overall, although applying a flat field correction compensates for the variation in intensity due to the pixel size no longer being constant across the sensor, it does not correct for the geometric distortions due to variations in shape of the pixels caused by skewness of the sensor's electric field. Consequently, artefacts are introduced and features in the images recorded by the GaAs:Cr device are distorted. Additionally, the flat field correction does not compensate for the fact that larger pixels that count more electrons will undercount electrons at lower electron fluences than is the case for smaller pixels. This lowers the maximum electron fluence that the detector can be exposed to without undercounting of electrons.

6. Conclusions

Our results confirm that high-Z sensors improve the performance of HPDs for high-energy electrons. When operating in SPM and using a high threshold, the GaAs:Cr Medipix3 device that we have characterised is able to match and surpass the performance expected of a square pixel detector in terms of its MTF for electrons with energies in the range of 60–200 keV. Using a high threshold has a negative effect on the device DQE, however, while using a low threshold significantly improves the GaAs:Cr SPM DQE for 120 keV and 200 keV electrons at high values of ω. This low threshold DQE of the GaAs:Cr detector for 200 keV electrons compares favourably with the DQE of the Falcon 3 MAPS detector for electrons of the same energy [23], though it should be noted that ω_N for the monolithic device is higher than that of the Medipix3 due to its smaller pixels.

Although the GaAs:Cr device outperforms the Si device for high-energy electrons, for electron energies below 120 keV, its performance in terms of DQE is poorer than that of the Si detector. This can be attributed to increased backscatter. Except for the most demanding of experimental conditions, there is likely to be minimal drawback in using the GaAs:Cr in experiments where it is necessary to use electrons with energies down to 60 keV. Our results also suggest that at lower energies there is the potential for a serious degradation in performance. As such, there is unlikely to be any advantage in the use of high-Z sensors for scanning electron microscopy or for use in TEM imaging using electrons with energies lower than 60 keV. However, it may be possible to improve the efficiency of the GaAs:Cr device at low energies if the frontside contact were made of a lower-Z material than Ni, such as Al, but this would require advances in device manufacture.

At the high-energy range considered in this work, the performance of the GaAs:Cr shows a significant performance loss for 300 keV electrons. This motivates the investigation of other sensor materials with even higher values of Z, such as CdTe and CZT (average Z = 50), though it is worth noting that using such materials will likely lead to further degradation in performance at low electron energies. No single imaging detector will perform ideally across all the electron energies typically used in transmission electron microscopy, but on the basis of our results, HPDs with GaAs:Cr sensors may offer the best performance over the widest range of accelerating voltages presently used in TEM. Although the performance of the GaAs:Cr sensor at 300 keV is poor, it is similar to that of the Si detector at 200 keV, and we note that Medipix3 devices with Si sensors, as well as similar HPDs with Si sensors are routinely used at 200 keV and 300 keV in a number of applications [15,18]. It is therefore likely that GaAs:Cr sensors can

be used with 300 keV electrons, offering improved MTF and DQE compared to a Si device used at 200 keV and 300 keV.

To determine how HPDs with high-Z sensors can be best utilised, it is helpful to discuss the optimal detector settings. It has been argued that for counting HPDs the optimum threshold is equal to half the primary electron energy so as to obtain the maximum enhancement of the MTF while minimising the negative the effects that using a high threshold has on the DQE. However, we argue that the choice of threshold should depend upon the constraints imposed by individual experiments. In situations where spatial resolution is of paramount importance and where there are no dose constraints then a high threshold that optimises the MTF can be used. For example, at a threshold of 104.4 keV the GaAs:Cr detector matches the best response of a square-pixel detector in terms of its MTF operating in SPM for 200 keV electron while its best MTF is obtained when using a threshold of 116.5 keV. The values of MTF(ω_N) for these thresholds are 2.5 and 3.0 times that obtained with the lowest threshold (12.7 keV) used. However, many of the experiments that DEDs enable are ones where dose is a constraint making detector efficiency key. In such cases, the corresponding decrease in DQE(ω_N) to 17.1% and 9.4% of its maximum value when these thresholds are used is likely to be unacceptable, particularly when information at high ω is important.

One class of experiments where high-Z sensors are likely to be particularly useful are time-resolved experiments. By reducing the lateral spread in the signal produced by the primary electrons, the temporal resolution of HPDs should be also be improved at high energies, as the scattering of incident electrons over multiple pixels means they can be counted in multiple frames when using short frame times [12]. Other experimental modes that would benefit from the use of HPDs with high-Z sensors include 4D-STEM modes that depend on precise measurement of the deflection of discs in the diffraction pattern due to either transmitted or Bragg-diffracted electrons. Precise measurements of such deflections can be achieved by template-matching [16,59], and, in principal, this kind of analysis and the automation thereof would benefit from an improved detector PSF. An enhanced PSF would also be beneficial for diffraction-based experiments where it is desirable to maximise the scattering angle subtended by the detector, and hence sampling of reciprocal space, by using a short camera-length while still clearly distinguishing between closely spaced diffraction spots or discs. Low-energy cryoEM is another application for which HPDs equipped with high-Z sensors are likely suitable on the basis of the low threshold DQE obtained for 80 keV and 120 keV electrons. This would require the field-of-view of HPDs be expanded, which can be done by tiling. The Medipix3 ASIC is buttable on 3 sides and can be used to create arrays that are 2×N in size (where N is an arbitrary number). One of its successors, Timepix4, in addition to having more pixels (448 × 512) is 4-side buttable, making it possible to create HPDs with similar numbers of pixels to monolithic devices [60]. Of course, the physical size of the detectors created by tiling that can be used is ultimately constrained by microscope design.

HPDs with high-Z sensors would be more suitable for applications requiring high spatial resolution and a large field-of-view if the entry point of incident electrons can be localised in a way that does not have a detrimental effect on DQE, particularly if this can be done to sub-pixel accuracy. CSM fails to consistently identify the entry pixel for both devices, though there are cases for which using CSM could be regarded as advantageous. For instance, when using 200 keV electrons, the low threshold GaAs:Cr CSM MTF(ω_N) is 0.41. The threshold at which the SPM MTF(ω_N) is equal to this is 64.6 keV, at which DQE(0) is 0.68 and DQE(ω_N) is 0.15, while the low threshold CSM DQE(0) and DQE(ω_N) are 0.91 and 0.10. Using CSM is therefore able to provide the same MTF and comparable high-frequency DQE while enhancing the low-frequency DQE compared with using SPM.

Nevertheless, our results confirm the need for more sophisticated approaches to localise the entry point of the electron tailored to electrons with energies typically used in TEM. CSM was developed with photons in mind, with the expectation that they would be counted by at most 4 pixels when they deposited their energy, via photoelectric absorption, in the corner of the entry pixel due to the lateral spread of the charge carriers in the sensor. Localising the entry point of electrons is far more challenging due to the stochastic way in which they deposit energy in the sensor, though the identification of the entry point of the electron to sub-pixel accuracy has proven possible with monolithic devices [36,51,61], and research into how to achieve superresolution with other types of DEDs is an active field [55,56]. Recent work with a Timepix3 detector with Si sensor has confirmed that it is possible to significantly enhance the MTF of HPDs for 200 keV and 300 keV electrons by identifying the entry pixel using a convolutional neural network [62]. However, it is not clear whether reducing the scatter of incident electrons in the sensor by using high-Z sensors will facilitate localisation of the entry point to sub-pixel accuracy, or if the loss of information about the electron trajectory will make this task more difficult.

Our work clarifies the advantages of a GaAs:Cr sensor compared to traditional Si sensors and also highlights the effects of the distortions that defects in the GaAs:Cr sensor introduce into the images recorded. Similar defects have been observed in other high-Z sensor materials, such as CdTe and CZT [63–65]. To maximise the potential benefits of high-Z sensors these defects must be addressed, either by correcting these by post-processing or by further fabrication development. Given the technical challenges improving the manufacture high-Z semiconductors suitable for radiation detection present, the former is a more viable solution in the short to mid-term.

Declaration of competing interest

The authors declare that they have no known competing financial interests or personal relationships that could have appeared to influence the work reported in this paper.

Data availability

The data presented in this article are available at http://dx.doi.org/10.5525/gla.researchdata.1145.

Acknowledgments

The authors gratefully acknowledge funding from the UK Science and Technology Facilities Council through the Industrial Cooperative Awards in Science & Technology (CASE) studentship "Next^2 Detection - Investigation of Hybrid Pixel Detectors for Future Transmission Electron Microscopy Imaging" (grant no. ST/P002471/1). The authors are grateful to Ms Nadia Bassiri, Mr Michael Perreur-Lloyd and Mr David Doak for their help developing hardware to mount detectors on microscopes. X.M. thanks Deutsche Forschungsgemeinschaft (DFG), Germany for funding (grant no. MU 4276/1-1). K.A.P. thanks Dr Anton Tyazhev and Ms Anastasia Lozinskaya of Tomsk State University for helpful discussions regarding the GaAs:Cr sensors. K.A.P. also thanks Dr Gary W. Paterson for helpful discussions regarding the calculation of the detectors' noise profiles. The authors are grateful to Karlsruhe Nano Micro Facility (KNMF), Germany for access to the FEI Titan 80 – 300 (S)TEM, and K.A.P and D.McG. acknowledge Quantum Detectors Ltd., UK for funding travel to KNMF as part of the Industrial CASE studentship that supports K.A.P. The authors also thank Quantum Detectors Ltd. for the loan of the Si Medipix3 device characterised as part this work. This work has been carried out within the framework of the Medipix3 collaboration.

Appendix A. Supplementary data

Supplementary material related to this article can be found online at https://doi.org/10.1016/j.ultramic.2021.113298.

References

[1] A. Merk, A. Bartesaghi, S. Banerjee, V. Falconieri, P. Rao, M.I. Davis, R. Pragani, M.B. Boxer, L.A. Earl, J.L.S. Milne, S. Subramaniam, Breaking cryo-EM resolution barriers to facilitate drug discovery, Cell 165 (7) (2016).

[2] Y. Jiang, Z. Chen, Y. Han, P. Deb, H. Gao, S. Xie, P. Purohit, M.W. Tate, J. Park, S.M. Gruner, V. Elser, D.A. Muller, Electron ptychography of 2D materials to deep sub-ångström resolution, Nature 559 (7714) (2018).

[3] G. McMullan, A.T. Clark, R. Turchetta, A.R. Faruqi, Enhanced imaging in low dose electron microscopy using electron counting, Ultramicroscopy 109 (12) (2009).

[4] J. Song, C.S. Allen, S. Gao, C. Huang, H. Sawada, X. Pan, J. Warner, P. Wang, A.I. Kirkland, Atomic resolution defocused electron ptychography at low dose with a fast, direct electron detector, Sci. Rep. 9 (1) (2019).

[5] Z. Chen, M. Weyland, C. Zheng, M.S. Fuhrer, A.J. D'Alfonso, L.J. Allen, S.D. Findlay, Facilitating Quantitative Analysis of Atomic Scale 4D STEM Datasets, Microsc. Microanal. 22 (S3) (2016).

[6] X.C. Bai, C. Yan, G. Yang, P. Lu, D. Ma, L. Sun, R. Zhou, S.H. Scheres, Y. Shi, An atomic structure of human γ-secretase, Nature 525 (7568) (2015).

[7] X. Li, P. Mooney, S. Zheng, C.R. Booth, M.B. Braunfeld, S. Gubbens, D.A. Agard, Y. Cheng, Electron counting and beam-induced motion correction enable near-atomic-resolution single-particle cryo-EM, Nat. Methods 10 (6) (2013).

[8] E. Frojdh, R. Ballabriga, M. Campbell, M. Fiederle, E. Hamann, T. Koenig, X. Llopart, D. de Paiva Magalhaes, M. Zuber, Count rate linearity and spectral response of the Medipix3RX chip coupled to a 300μm silicon sensor under high flux conditions, J. Instrum. 9 (4) (2014).

[9] M.W. Tate, P. Purohit, D. Chamberlain, K.X. Nguyen, R. Hovden, C.S. Chang, P. Deb, E. Turgut, J.T. Heron, D.G. Schlom, D.C. Ralph, G.D. Fuchs, K.S. Shanks, H.T. Philipp, D.A. Muller, S.M. Gruner, High Dynamic Range Pixel Array Detector for Scanning Transmission Electron Microscopy, Microsc. Microanal. 22 (1) (2016).

[10] A.I. Kirkland, C.S. Allen, E. Besley, C. Huang, J. Kim, S. Skowron, J. Warner, Observing Structural Dynamics and Measuring Chemical Kinetics in Low Dimensional Materials Using High Speed Imaging, Microsc. Microanal. 25 (S2) (2019) 1682–1683.

[11] R. Beacham, A.M. Raighne, D. Maneuski, V. O'Shea, S. McVitie, D. McGrouther, Medipix2/Timepix Detector for time resolved Transmission Electron microscopy, J. Instrum. 6 (12) (2011).

[12] G.W. Paterson, R.J. Lamb, R. Ballabriga, D. Maneuski, V. O'Shea, D. McGrouther, Sub-100 nanosecond temporally resolved imaging with the Medipix3 direct electron detector, Ultramicroscopy 210 (2020).

[13] G. Tinti, E. Frojdh, E. Van Genderen, T. Gruene, B. Schmitt, D.A. Matthijs De Winter, B.M. Weckhuysen, J.P. Abrahams, Electron crystallography with the EIGER detector, IUCrJ 5 (2) (2018).

[14] S. Fang, Y. Wen, C.S. Allen, C. Ophus, G.G.D. Han, A.I. Kirkland, E. Kaxiras, J.H. Warner, Atomic electrostatic maps of 1D channels in 2D semiconductors using 4D scanning transmission electron microscopy, Nature Commun. 10 (1) (2019).

[15] R.C. Temple, T.P. Almeida, J.R. Massey, K. Fallon, R. Lamb, S.A. Morley, F. Maccherozzi, S.S. Dhesi, D. McGrouther, S. McVitie, T.A. Moore, C.H. Marrows, Antiferromagnetic-ferromagnetic phase domain development in nanopatterned FeRh islands, Phys. Rev. Mater. 2 (10) (2018).

[16] M. Krajnak, D. McGrouther, D. Maneuski, V. O'Shea, S. McVitie, Pixelated detectors and improved efficiency for magnetic imaging in STEM differential phase contrast, Ultramicroscopy 165 (2016).

[17] R. Bücker, P. Hogan-Lamarre, P. Mehrabi, E.C. Schulz, L.A. Bultema, Y. Gevorkov, W. Brehm, O. Yefanov, D. Oberthür, G.H. Kassier, R.J.D. Miller, R.J. Dwayne Miller, Serial protein crystallography in an electron microscope, Nature Commun. 11 (1) (2020).

[18] L. Zhou, J. Song, J.S. Kim, X. Pei, C. Huang, M. Boyce, L. Mendonça, D. Clare, A. Siebert, C.S. Allen, E. Liberti, D. Stuart, X. Pan, P.D. Nellist, P. Zhang, A.I. Kirkland, P. Wang, Low-dose phase retrieval of biological specimens using cryo-electron ptychography, Nature Commun. 11 (1) (2020).

[19] B. Plotkin-Swing, G.J. Corbin, S. De Carlo, N. Dellby, C. Hoermann, M.V. Hoffman, T.C. Lovejoy, C.E. Meyer, A. Mittelberger, R. Pantelic, L. Piazza, O.L. Krivanek, Hybrid pixel direct detector for electron energy loss spectroscopy, Ultramicroscopy (2020).

[20] A.R. Faruqi, R. Henderson, M. Pryddetch, P. Allport, A. Evans, Direct single electron detection with a CMOS detector for electron microscopy, Nucl. Instrum. Methods Phys. Res. Sect. A: 546 (1–2) (2005).

[21] A. Milazzo, P. Leblanc, F. Duttweiler, L. Jin, J.C. Bouwer, S. Peltier, M. Ellisman, F. Bieser, H.S. Matis, H. Wieman, P. Denes, S. Kleinfelder, N. Xuong, Active pixel sensor array as a detector for electron microscopy, Ultramicroscopy 104 (2) (2005).

[22] G. McMullan, A.R. Faruqi, R. Henderson, N. Guerrini, R. Turchetta, A. Jacobs, G. van Hoften, Experimental observation of the improvement in MTF from backthinning a CMOS direct electron detector, Ultramicroscopy 109 (9) (2009).

[23] M. Kuijper, G. van Hoften, B. Janssen, R. Geurink, S. De Carlo, M. Vos, G. van Duinen, B. van Haeringen, M. Storms, FEI's direct electron detector developments: Embarking on a revolution in cryo-TEM, J. Struct. Biol. 192 (2) (2015).

[24] M.J. Peet, R. Henderson, C.J. Russo, The energy dependence of contrast and damage in electron cryomicroscopy of biological molecules, Ultramicroscopy 203 (2019).

[25] K. Naydenova, G. McMullan, M.J. Peet, Y. Lee, P.C. Edwards, S. Chen, E. Leahy, S. Scotcher, R. Henderson, C.J. Russo, CryoEM At 100 keV: a demonstration and prospects, IUCrJ 6 (6) (2019).

[26] R.F. Egerton, P. Li, M. Malac, Radiation damage in the TEM and SEM, Micron 35 (6) (2004).

[27] S. Cheng, A. Pofelski, P. Longo, R.D. Twesten, Y. Zhu, G.A. Botton, The performance evaluation of direct detection electron energy-loss spectroscopy at 200 kV and 80 kV accelerating voltages, Ultramicroscopy 212 (2020).

[28] J. Ciston, I.J. Johnson, B.R. Draney, P. Ercius, E. Fong, A. Goldschmidt, J.M. Joseph, J.R. Lee, A. Mueller, C. Ophus, A. Selvarajan, D.E. Skinner, T. Stezelberger, C.S. Tindall, A.M. Minor, P. Denes, The 4D Camera: Very High Speed Electron Counting for 4D-STEM, Microsc. Microanal. 25 (S2) (2019).

[29] T. Poikela, J. Plosila, T. Westerlund, M. Campbell, M.D. Gaspari, X. Llopart, V. Gromov, R. Kluit, M. van Beuzekom, F. Zappon, V. Zivkovic, C. Brezina, K. Desch, Y. Fu, A. Kruth, Timepix3: A 65k channel hybrid pixel readout chip with simultaneous ToA/ToT and sparse readout, J. Instrum. 9 (5) (2014).

[30] W. Gao, C. Addiego, H. Wang, X. Yan, Y. Hou, D. Ji, C. Heikes, Y. Zhang, L. Li, H. Huyan, T. Blum, T. Aoki, Y. Nie, D.G. Schlom, R. Wu, X. Pan, Real-space charge-density imaging with sub-ångström resolution by four-dimensional electron microscopy, Nature 575 (7783) (2019).

[31] M. Gallagher-Jones, C. Ophus, K.C. Bustillo, D.R. Boyer, O. Panova, C. Glynn, C.T. Zee, J. Ciston, K.C. Mancia, A.M. Minor, J.A. Rodriguez, Nanoscale mosaicity revealed in peptide microcrystals by scanning electron nanodiffraction, Commun. Biol. 2 (1) (2019).

[32] R. Ballabriga, J. Alozy, G. Blaj, M. Campbell, M. Fiederle, E. Frojdh, E.H.M. Heijne, X. Llopart, M. Pichotka, S. Procz, L. Tlustos, W. Wong, The Medipix3RX: a high resolution, zero dead-time pixel detector readout chip allowing spectroscopic imaging, J. Instrum. (2013).

[33] J.A. Mir, R. Clough, R. MacInnes, C. Gough, R. Plackett, I. Shipsey, H. Sawada, I. MacLaren, R. Ballabriga, D. Maneuski, V. O'Shea, D. McGrouther, A.I. Kirkland, Characterisation of the medipix3 detector for 60 and 80 keV electrons, Ultramicroscopy 182 (2017).

[34] G. McMullan, D.M. Cattermole, S. Chen, R. Henderson, X. Llopart, C. Summerfield, L. Tlustos, A.R. Faruqi, Electron imaging with Medipix2 hybrid pixel detector, Ultramicroscopy 107 (4–5) (2007).

[35] G. McMullan, A.R. Faruqi, Electron microscope imaging of single particles using the Medipix2 detector, Nucl. Instrum. Methods Phys. Res. Sect. A 591 (1) (2008).

[36] G. McMullan, S. Chen, R. Henderson, A.R. Faruqi, Detective quantum efficiency of electron area detectors in electron microscopy, Ultramicroscopy 109 (9) (2009).

[37] R. Plackett, I. Horswell, E.N. Gimenez, J. Marchal, D. Omar, N. Tartoni, Merlin: a fast versatile readout system for Medipix3, J. Instrum. 8 (01) (2013).

[38] A.V. Tyazhev, D.L. Budnitsky, O.B. Koretskay, V.A. Novikov, L.S. Okaevich, A.I. Potapov, O.P. Tolbanov, A.P. Vorobiev, GaAs Radiation imaging detectors with an active layer thickness up to 1 mm, Nucl. Instrum. Methods Phys. Res. Sect. A 509 (1–3) (2003).

[39] L. Tlustos, M. Campbell, C. Fröjdh, P. Kostamo, S. Nenonen, Characterisation of an epitaxial GaAs/Medipix2 detector using fluorescence photons, Nucl. Instrum. Methods Phys. Res. Sect. A 591 (1) (2008).

[40] T.E. Schlesinger, J.E. Toney, H. Yoon, E.Y. Lee, B.A. Brunett, L. Franks, R.B. James, Cadmium zinc telluride and its use as a nuclear radiation detector material, Mater. Sci. Eng. R 32 (4–5) (2001).

[41] A. Tyazhev, D. Budnitsky, D. Mokeev, V. Novikov, A. Zarubin, O. Tolbanov, G. Shelkov, E. Hamann, A. Fauler, M. Fiederle, S. Procz, GaAs Pixel detectors, Int. J. Microwave Wirel. Technol. 1576 (1) (2013).

[42] A. Tyazhev, V. Novikov, O. Tolbanov, A. Zarubin, M. Fiederle, E. Hamann, Investigation of the current-voltage characteristics, the electric field distribution and the charge collection efficiency in x-ray sensors based on chromium compensated gallium arsenide, Hard X-Ray, Gamma-Ray, and Neutron Detector Physics XVI 9213 (2014).

[43] E. Hamann, T. Koenig, M. Zuber, A. Cecilia, A. Tyazhev, O. Tolbanov, S. Procz, A. Fauler, T. Baumbach, M. Fiederle, Performance of a Medipix3RX Spectroscopic Pixel Detector With a High Resistivity Gallium Arsenide Sensor, IEEE Trans. Med. Imaging 34 (3) (2015).

[44] M.C. Veale, S.J. Bell, D.D. Duarte, M.J. French, A. Schneider, P. Seller, M.D. Wilson, A.D. Lozinskaya, V.A. Novikov, O.P. Tolbanov, A. Tyazhev, A.N. Zarubin, Chromium compensated gallium arsenide detectors for X-ray and γ-ray spectroscopic imaging, Nucl. Instrum. Methods Phys. Res. Sect. A 752 (2014).

[45] J. Becker, M.W. Tate, K.S. Shanks, H.T. Philipp, J.T. Weiss, P. Purohit, D. Chamberlain, S.M. Gruner, Characterization of chromium compensated GaAs as an X-ray sensor material for charge-integrating pixel array detectors, J. Instrum. 13 (1) (2018).

[46] M.C. Veale, S.J. Bell, D.D. Duarte, M.J. French, M. Hart, A. Schneider, P. Seller, M.D. Wilson, V. Kachkanov, A.D. Lozinskaya, V.A. Novikov, O.P. Tolbanov, A. Tyazhev, A.N. Zarubin, Investigating the suitability of GaAs:Cr material for high flux X-ray imaging, J. Instrum. 9 (12) (2014).

[47] A. Schneider, M.C. Veale, D.D. Duarte, S.J. Bell, M.D. Wilson, J.D. Lipp, P. Seller, Interconnect and bonding techniques for pixelated X-ray and gamma-ray detectors, 2015.
[48] I.A. Cunningham, Chapter 2: Applied Linear-Systems Theory, in: R.L. Van Metter, J. Beutel, H.L. Kundel (Eds.), Handbook of Medical Imaging, Volume 1: Physics and Psychophysics, SPIE, 2000.
[49] C.E. Metz, K. Doi, Transfer function analysis of radiographic imaging systems, Phys. Med. Biol. 24 (6) (1979).
[50] R.R. Meyer, A.I. Kirkland, Characterisation of the signal and noise transfer of CCD cameras for electron detection, Microsc. Res. Tech. 49 (3) (2000).
[51] R.S. Ruskin, Z. Yu, N. Grigorieff, Quantitative characterization of electron detectors for transmission electron microscopy, J. Struct. Biol. 184 (3) (2013).
[52] M. Battaglia, D. Contarato, P. Denes, D. Doering, T. Duden, B. Krieger, P. Giubilato, D. Gnani, V. Radmilovic, Characterisation of a CMOS active pixel sensor for use in the TEAM microscope, Nucl. Instrum. Methods Phys. Res. Sect. A 622 (3) (2010).
[53] G. Deptuch, A. Besson, P. Rehak, M. Szelezniak, J. Wall, M. Winter, Y. Zhu, Direct electron imaging in electron microscopy with monolithic active pixel sensors, Ultramicroscopy 107 (8) (2007).
[54] W. Zhao, J.A. Rowlands, Digital radiology using active matrix readout of amorphous selenium: Theoretical analysis of detective quantum efficiency, Med. Phys. 24 (12) (1997).
[55] H. Ryll, M. Huth, R. Ritz, C.M. O'Leary, I. Griffiths, P. Nellist, R. Sagawa, Y. Kondo, H. Soltau, L. Strüder, Measuring Single Electrons – What Does it Mean? Microsc. Microanal. 25 (S2) (2019).
[56] G. Correa, D. Muller, Machine Learning for Sub-pixel Super-resolution in Direct Electron Detectors, Microsc. Microanal. (2020).
[57] P. Rudolph, Dislocation cell structures in melt-grown semiconductor compound crystals, Cryst. Res. Technol. 40 (1–2) (2005).
[58] C. Frank-Rotsch, U. Juda, F.-M. Kiessling, P. Rudolph, Dislocation patterning during crystal growth of semiconductor compounds (GaAs), Mater. Sci. Technol. 21 (12) (2005).
[59] S.E. Zeltmann, A. Müller, K.C. Bustillo, B. Savitzky, L. Hughes, A.M. Minor, C. Ophus, Patterned probes for high precision 4D-STEM bragg measurements, Ultramicroscopy 209 (2020) 112890.
[60] R. Ballabriga, M. Campbell, X. Llopart, An introduction to the Medipix family ASICs, Radiat. Meas. 136 (2020).
[61] P.L. Chiu, X. Li, Z. Li, B. Beckett, A.F. Brilot, N. Grigorieff, D.A. Agard, Y. Cheng, T. Walz, Evaluation of super-resolution performance of the K2 electron-counting camera using 2D crystals of aquaporin-0, Journal of Structural Biology 192 (2) (2015).
[62] J.P. van Schayck, E. van Genderen, E. Maddox, L. Roussel, H. Boulanger, E. Fröjdh, J.-P. Abrahams, P.J. Peters, R.B. Ravelli, Sub-pixel electron detection using a convolutional neural network, Ultramicroscopy (2020).
[63] D. Pennicard, S. Smoljanin, B. Struth, H. Hirsemann, A. Fauler, M. Fiederle, O. Tolbanov, A. Zarubin, A. Tyazhev, G. Shelkov, H. Graafsma, The LAMBDA photon-counting pixel detector and high-Z sensor development, J. Instrum. 9 (12) (2014).
[64] D. Maneuski, V. Astromskas, E. Fröjdh, C. Fröjdh, E.N. Gimenez, J. Marchal, V. O'Shea, G. Stewart, N. Tartoni, H. Wilhelm, K. Wraight, R.M. Zain, Imaging and spectroscopic performance studies of pixellated CdTe timepix detector, J. Instrum. 7 (1) (2012).
[65] M.C. Veale, P. Booker, S. Cross, M.D. Hart, L. Jowitt, J. Lipp, A. Schneider, P. Seller, R.M. Wheater, M.D. Wilson, C.C.T. Hansson, K. Iniewski, P. Marthandam, G. Prekas, Characterization of the uniformity of high-flux CdZnTe Material, Sensors 20 (10) (2020).